2016 IEEE/RSJ International Conference on Intelligent Robots and Systems (IROS)
Daejeon Convention Center
October 9-14, 2016, Daejeon, Korea

SUAV:Q - An Improved Design for a Transformable Solar-Powered UAV

Ruben D'Sa, Devon Jenson, Travis Henderson, Jack Kilian, Bobby Schulz,
Michael Calvert, Thaine Heller, and Nikolaos Papanikolopoulos
{dsaxx005 | jens1172 | hende471 | kilia025 | schu3119 | calve046 | helle219}@umn.edu, {npapas}@cs.umn.edu
Department of Computer Science and Engineering, University of Minnesota

Abstract— **Throughout the wide range of aerial robot related applications, selecting a particular airframe is often a trade-off. Fixed-wing small-scale unmanned aerial vehicles (UAVs) typically have difficulty surveying at low altitudes while quad-rotor UAVs, having more maneuverability, suffer from limited flight time. Recent prior work [1] proposes a solar-powered small-scale aerial vehicle designed to transform between fixed-wing and quad-rotor configurations. Surplus energy collected and stored while in a fixed-wing configuration is utilized while in a quad-rotor configuration.**

This paper presents an improvement to the robot's design in [1] by pursuing a modular airframe, an optimization of the hybrid propulsion system, and solar power electronics. Two prototypes of the robot have been fabricated for independent testing of the airframe in fixed-wing and quad-rotor states. Validation of the solar power electronics and hybrid propulsion system designs were demonstrated through a combination of simulation and empirical data from prototype hardware.

I. INTRODUCTION

The domain of unmanned aerial vehicles (UAVs) has grown tremendously across a variety of disciplines in both academic and industrial settings, thanks in part to the availability of affordable sensors, actuators, and flight controllers. The fundamental design of UAVs have seen major leaps in development, most notability in the area of small-scale airframes. Research on small-scale airframes have taken many forms: from sensor applications in [2], [3], [4], to highly maneuverable systems in [5]. A number of systems have also been designed to leverage solar power collection to facilitate day-long and multi-day flight [6], [7], [8].

The concept and development of a small-scale solar-powered UAV capable of transforming between quad-rotor and fixed-wing states was presented in [1]. An energy framework was also showcased, providing the fundamental basis for augmented energy management. In contrast to a number of vertical-takeoff-and-landing (VTOL) airframe designs discussed in [9], the aircraft design of the SUAV:Q combines the stability and compactness of a quad-rotor with the efficient solar-powered flight capabilities of a high aspect ratio flying wing. By transitioning between quad-rotor and fixed-wing states, the system is capable of daylong flight while simultaneously achieving mission specific tasks such as maximizing the flight time spent in a quad-rotor state.

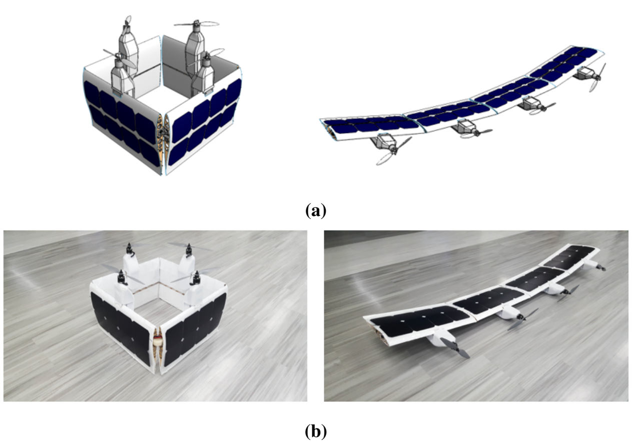
(a)
(b)

Fig. 1: (a) CAD model of the SUAV:Q airframe in both quad-rotor and fixed-wing configurations. (b) A single prototype was constructed to demonstrate stable functionality in quad-rotor and fixed-wing states.

A number of improvements to [1] are presented in this paper. Specifically, these improvements address a more modular aircraft and payload design, an optimization of the propulsion system design through the introduction of an additional degree of actuation, and the design, simulation, and an evaluation of an optimized solar power electronics system.

II. ROBOT DESIGN

This section discusses an updated evaluation of the aircraft design and performance from [1] as well as the design, simulation, and empirical results from the hybrid propulsion and power electronics systems.

A. Aircraft Design

To facilitate carrying a variety of sensor payloads and battery sizes along with supporting the flight characteristics of the aircraft in fixed-wing mode, the module enclosure shown in Figure 2 was designed. Components in each module are identical across wing sections with the exception of the two outer modules which exchange the Pixhawk and GPS components with a servo for driving the aircraft control surfaces. Due to the limited airframe volume of flying wing designs, along with the necessity to access internal electronics and sensors, the module was designed to be removable through two fasteners on the frame mount shown in Figure 3. Additional space inside of the module enclosure provides flexibility with regard to center of gravity placement. One of the design considerations for the enclosure was to make it printable on widely available consumer fused-deposition modeling (FDM) 3D printers. The intent of this design strategy was to facilitate adoption of the SUAV:Q platform by offering easily customizable and modular designs for researchers to use across various disciplines.

978-1-5090-3762-9/16/$31.00 ©2016 IEEE

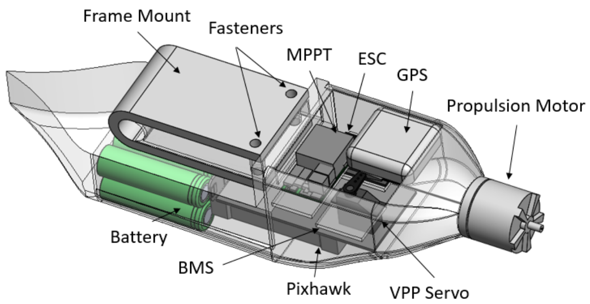

Fig. 2: Module enclosure containing the maximum power point tracker (MPPT), electronic speed controller (ESC), batteries, variable pitch propeller (VPP) servo, battery management system (BMS), Pixhawk autopilot and GPS.

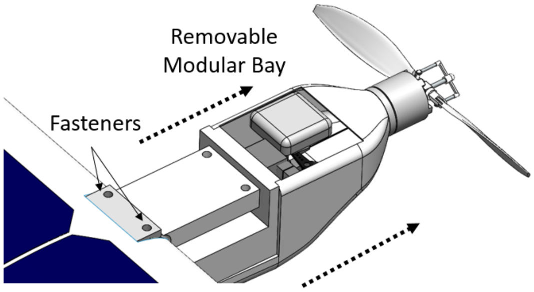

Fig. 3: 3D printed modular equipment and payload bay, designed to be readily swappable in the field and printable on a consumer grade FDM 3D printer.

To understand the consequence of varying the location of the center of gravity (CG) in each of the individual airframe sections, the entire fixed-wing airframe was simulated in XFLR5 [10] via vortex lattice method fixed lift analysis. Flight polars were collected over a range of CG locations that constitute potential stable operating conditions. Shown in Figure 4 is a side profile view of a wing section with CG and the neutral point (NP) locations denoted. The open circles in Figure 5(a) highlight the point where the aircraft with a given CG location will fly at a level altitude due to a neutral pitching moment. As the location of the CG moves further away from the NP, the necessary cruise velocity for level flight increases, raising the power consumption and hardware requirements of the propulsion system. Moving the CG closer to the NP reduces the necessary cruise velocity at the expense of pitch stability in turbulent conditions.

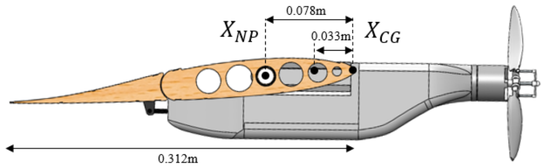

Fig. 4: Locations of the neutral point (X_{NP}) and center of gravity (X_{CG}) of an individual wing segment. The SUAV:Q platform has a total mass of 4.93kg.

In the process of developing custom modules for various operating conditions, prescribing the orientation of the wing with respect to the propulsion system is crucial. Figure 5(b) is used to determine, given a particular CG location, the necessary angle of incidence between the propulsion system and wing to provide a neutral pitching moment.

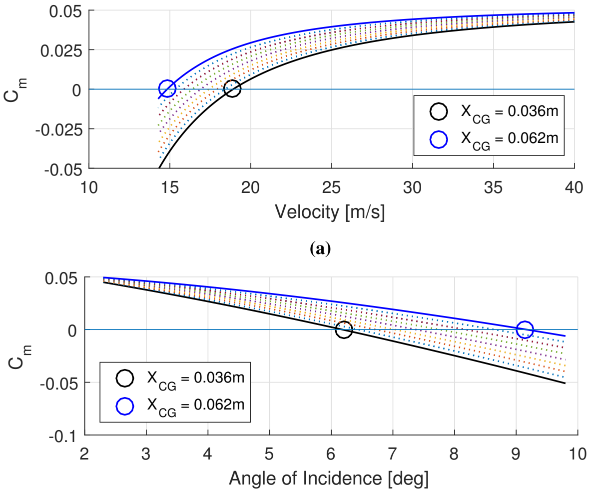

(a)

(b)

Fig. 5: (a) C_m represents the moment coefficient of the airframe evaluated using the full SUAV:Q airframe [1] in XFLR5 with respect to velocity. (b) Angle of incidence necessary to provide a neutral pitching moment. Simulations were performed with a constant system mass of 4.93 kg. X_{CG} is measured with respect to the leading edge with positive distance in the direction of the tailing edge.

For high efficiency in both the fixed-wing and multi-rotor states, the airframe structure was fabricated using basswood ribs mounted on a carbon fiber spar. Additional strength was given in the form of carbon fiber stringers, parallel to the spars. A sheet of balsa was added to the top surface of the wing underneath the polystyrene coating, to provide backing for the solar cells and added strength. To reduce weight, the basswood ribs were perforated with circular cutouts along the camber line.

Transformation hinges of the aircraft are based off work from [1], utilizing a servo driven 4-bar linkage mechanism. As shown in Figure 6, the graphically synthesized mechanism leverages a deadpoint in quad-rotor state and a hard-stop in fixed-wing state to minimize actuator power consumption. Control of the hinges is managed by the Pixhawk autopilot, toggling between each state by commanding the corresponding state positions through PWM.

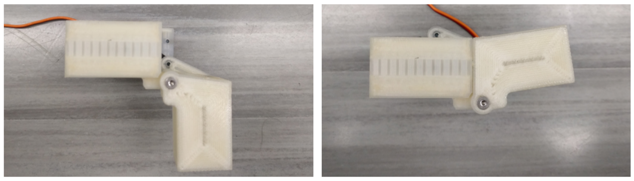

Fig. 6: Servo driven 4-bar hinge in quad-state (left) and fixed-wing (right).

To provide control authority without compromising solar collection surface area, the inner segments were sized to accommodate the full chordwise length of the solar array, and the outer segments were designed to have control surfaces large enough to fit four SunPower E60 solar cells. The remaining fixed portion holds an additional four solar cells, for a total of 8 solar cells per wing segment and 32 solar cells over the entire airframe.

B. Hybrid Propulsion System

The goal in designing a single-mode, solar-powered aircraft is to optimize the aircraft's efficiency close to the characteristic operating point, usually level flight [8]. In the case of the SUAV:Q, the introduction of a second characteristic operating point creates an enlarged flight envelope, and fixed-geometry propellers do not efficiently meet the associated propulsion demands [11]. To illustrate, Figure 7 shows the performance characteristics of an APC 10 in. x 4.7 in. Slow Flyer (APC 10x4.7SF) propeller, chosen for analysis because of its acceptable efficiency over a wide range of flight conditions [12]. The dimensionless values J (advance ratio), C_T (coefficient of thrust), and C_P (coefficient of power) are calculated according to [11]:

$$J = \frac{V_{axial}}{nD} \tag{1}$$

$$C_T = \frac{T}{\rho n^2 D^4} \tag{2}$$

$$C_P = \frac{P_{shaft}}{\rho n^3 D^5} \tag{3}$$

where V_{axial} is the velocity of the aircraft in the thrust direction, n is the propeller rotational velocity, D is the propeller diameter, T is the propeller thrust, ρ is the density of air, and P_{shaft} is the mechanical power at the output shaft of the motor.

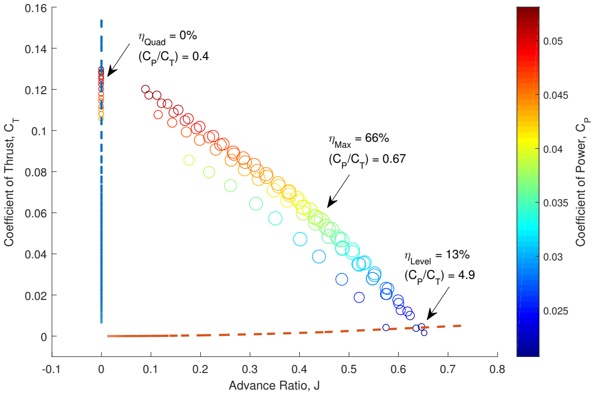

Fig. 7: Dimensionless plot of performance data of APC 10x4.7SF propeller. Aerodynamic efficiency η is represented by the size of the data point, where a large point denotes high efficiency. The data points which are down and to the left of the main trend were taken at a lower propeller speed of about 4000 rpm, and thus exhibit reduced performance due to Reynolds number effects [12].

By applying Newton's second law to a free-body diagram of the SUAV:Q, the thrust requirements and flight speeds can be estimated for level flight and hover conditions. The red line above the x-axis in Figure 7 shows the solution set of possible propeller states which satisfies the SUAV:Q thrust and flight speed requirements for level flight, and the blue line to the right of the y-axis of the same figure shows the possible propeller states satisfying hover in quad-rotor mode. The intersections of the blue and red curves with the propeller data mark the propeller states for which the propeller could theoretically satisfy the propulsion requirements for hover and level flight, respectively. Notice, however, that the SUAV:Q characteristic flight conditions occur at the extremities of the propeller's performance data, and that in level flight the propeller can neither convert power efficiently (shown by the low value of η) nor effectively produce thrust (high value of $\frac{C_P}{C_T}$). These observations strongly suggest that power conservation in the SUAV:Q requires a flexible propulsion system that efficiently converts power throughout all operating conditions. In order to overcome the limitations of fixed-geometry propellers implied by Figure 7, a degree of freedom is introduced into the SUAV:Q propulsion system: real-time control of the propeller's pitch angle.

The aerodynamic characteristics of a propeller are defined primarily by its three-dimensional geometry. Combining this geometric knowledge with the magnitude and direction of airflow past the blades allows a complete propulsive description of the propeller's state to be specified. When propeller blade pitch β is allowed to vary as shown in Figure 8 in addition to a variable propeller speed, the two-degree-of-freedom system can be varied in order to find the point at which a thrust constraint is satisfied at a minimum energy cost.

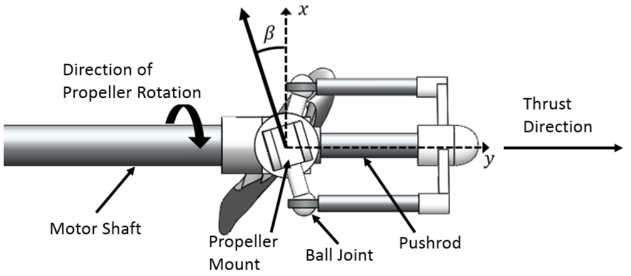

Fig. 8: Variable pitch control mechanism used in the hybrid propulsion system. A linkage connects the propeller mount to a pushrod that is concentric with the motor shaft. Note that β is defined in this paper as the angle through which the original propeller blade would rotate in order to achieve a desired orientation. This definition is convenient when referring to the propeller blade as a whole.

In order to investigate the value of this hybrid propulsion system, a numerical simulation of a variable pitch propeller (VPP) was constructed. The core of the simulation was executed by QPROP, a propeller analysis tool developed in [13]. MATLAB code was written to prepare flight simulation scenarios, send and receive data from QPROP, and organize the resulting aerodynamic information into graphical form. During formulation of flight scenarios, it was assumed that air was at standard temperature and pressure and that atmospheric air speed was zero with respect to an inertial reference frame. A level-flight dynamics model was developed according to [14] and aircraft drag was estimated with the airfoil analysis tool XFOIL [15].

Required thrust was assumed to be split equally among four motor-propeller pairs. Control of the VPP was modeled such that the optimum offset angle could be resolved instantaneously to better than 0.1°. Figure 9 shows the results of a simulation of the SUAV:Q performing a simple sequence of kinematic altitude commands in quad-rotor mode.

The simulation was conducted twice; the first iteration used a model of the off-the-shelf APC 10x4.7SF propeller employed in Figure 7. The second iteration of the simulation

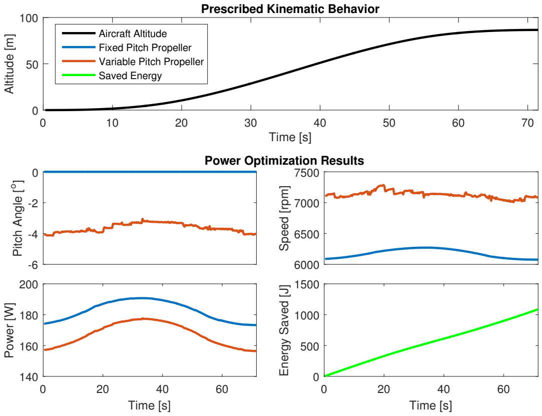

Fig. 9: Data obtained from a power optimization simulation on β for an SUAV:Q airframe weight of 4.93 kg. The electrical input power shown on the y-axis of the bottom-left frame was obtained by applying a model of a MT2814 770 Kv electric motor into QPROP to calculate input electrical power. The noise seen throughout the second row of plots is due to the implementation of the global Newton method QPROP uses to solve the system of equations modeling the propeller [13].

scenario varied the pitch angle of the propeller in order to converge on a solution which satisfied the kinematic constraints at the minimum value of P_{shaft}.

While shaft power is the quantity which corresponds to the power-optimal pitch angle, the amount of energy saved corresponds to the amount of power drawn from electrical power sources. The bottom-right frame of Figure 7 shows the amount of electrical energy that the VPP saves compared with the energy used by the fixed-pitch propeller according to

$$E_{saved} = \int_{t_0}^{t} (P_{fixed} - P_{variable})dt \tag{4}$$

Under the conditions specified, the average power savings in quad-rotor mode is over 17 W per motor, leading to an overall savings of almost 70 W, or about a 10% reduction in power consumption for hover. Simulations were also run in order to calculate the amount of power saved in level flight. The average power savings in level flight was almost 15 W per motor, which translates to approximately a 50% reduction in level-flight power when compared with the level-flight power under a fixed-pitch simulation.

C. Power Electronics Design

In many applications, the sole purpose of power electronics is to efficiently convert from one form of power to another. For this reason, there are many off-the-shelf solutions that can be readily incorporated into existing systems. However, even with this large selection, it is difficult to find an effective solution when the power electronics are an integral part of system operation. In solar-powered aircraft, especially those designed for long-term autonomous operation, the system must be "energy aware" and change its behavior in order to maximize the availability of solar power. The maximum power point tracker (MPPT) module must not only be able to efficiently track and manage solar power, but also communicate with other system modules. Shared information can be used to optimize performance and make predictions about future conditions. For example, solar availability data could be incorporated into path planning and aircraft orientation could be used to optimize the MPPT algorithm. Figure 10 shows the interconnection between electrical modules of the SUAV:Q.

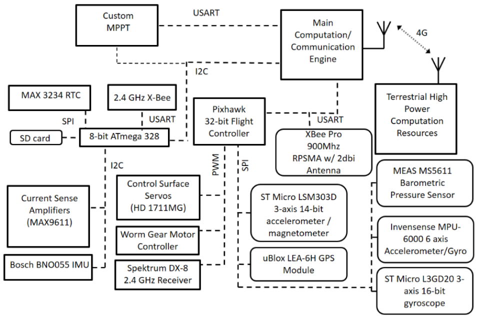

Fig. 10: SUAV:Q electrical communication topology.

To avoid the power tracking issues associated with solar cells experiencing non-uniform solar irradiance, the solar cells should be wired in series with neighboring solar cells on individual wing sections. While it may be acceptable to use a single MPPT on a fixed-wing aircraft where the dihedral angles are relatively small (see Section III), this is not acceptable on the SUAV:Q due to the wide range of dihedral angles. In the worst case situation, solar panels are orthogonal to one another. Therefore, to maximize the availability of solar energy for any dihedral angle, the maximum power point (MPP) for each wing segment panel must be independently tracked. This reinforces the modular design of the SUAV:Q and requires the MPPT printed circuit board (PCB) to have a small form factor in order to fit in the wing segment module enclosure. The following section gives a brief overview of the custom MPPT design, taking into consideration efficiency, communication, and PCB size required by the SUAV:Q.

D. MPPT Hardware Design

The hardware of the MPPT depends on the input/output voltages and currents of the system. On the present SUAV:Q design, each wing segment fits eight solar cells. Using SunPower E60 cells connected in series, the maximum expected MPPT input voltage and current are 5.84 V and 6.17 A, respectively. Additionally, each wing segment contains a battery pack which consists of 8 NCR18650B batteries in a 2p4s configuration. Thus, the MPPT output voltage ranges from 8.4 V (minimum charge) to 16.8 V (maximum charge), as summarized in Table I.

TABLE I: MPPT Design Parameters

$V_{\text{in, max}}$	5.84 V
$I_{\text{in, max}}$	6.17 A
$V_{\text{out, max}}$	16.8 V
$V_{\text{out, min}}$	8.4 V

TABLE II: MPPT Component Values

C_{in}	66 μF
L	22 μH
M	IPT004N03L
D	PMEG045V100EPD
C_{out}	284 μF

Due to the input voltage of the solar array being lower than the discharged battery voltage, a standard (non-synchronous) boost topology was chosen for simple control (low-side gate driver) and small PCB footprint. The schematic is shown in Figure 11.

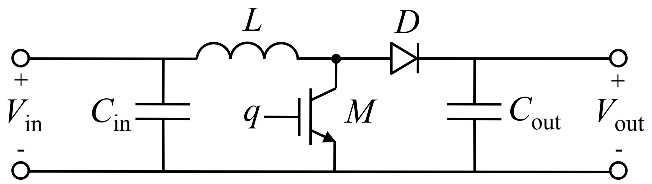

Fig. 11: Schematic of a basic boost converter. Signal q is the gate drive signal, determining the switching frequency ($\frac{1}{T_s}$) and duty ratio (d) of the converter.

The design parameters in Table I determine the required component values and minimum voltage/current ratings. A nominal switching frequency of 100 kHz was assumed. The component values used in the design are shown in Table II. These values allow for a small PCB size without sacrificing adequate filtering. See Section III for empirical results on the efficiency of the design. In particular, L was chosen for low ripple current defined in Equation 5 [16].

$$\Delta i_L = \frac{1}{L} V_{in} d T_s \tag{5}$$

Gate signal q is driven by a UCC27519A low-side gate driver. The signal is provided by a dsPIC33EV256GM102 microcontroller (MCU) running an MPPT tracking algorithm. The chosen algorithm can have a large impact on MPPT performance, especially in dynamic solar conditions as discussed in Section II-E. The MCU's on-board analog-to-digital converters (ADCs) are used to measure both input and output voltages as well as current using TI INA212 current sense amplifiers. The measured values are used by the chosen tracking algorithm to determine the MPP of a solar panel. In particular, the duty ratio d is selected to match the input equivalent resistance of the MPPT with the output resistance of the solar panels. With a boost converter topology, the equivalent resistance and voltage seen by the panel are given by Equations 6 and 7 from [17].

$$R_{in} = (1-d)^2 R_{load} \tag{6}$$

$$V_{in} = (1-d) V_{out} \tag{7}$$

The MCU provides various communication interfaces such as UART, I^2C, and SPI. Custom firmware allows for charge control of specific batteries and different MPPT algorithms in quad-rotor and fixed-wing states. Figure 12 shows the implementation of the custom MPPT as the 4-layer PCB.

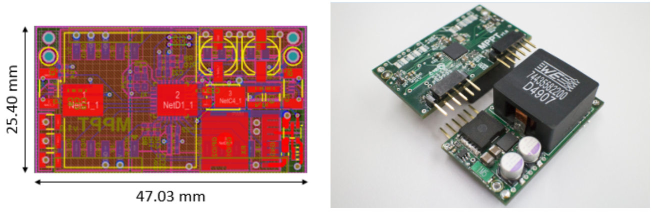

(a) **(b)**

Fig. 12: (a) The custom designed MPPT PCB utilizes a 4-layer design with ground and high power planes on the inner layers and signal planes on the outer most layers. (b) Fabricated custom MPPT prototype used in experimental data collection.

E. MPPT Algorithm: Perturb and Observe Approach

An MPPT algorithm is designed to maximize the power out of a solar array by adjusting the operating voltage at the terminals of a solar array. The most common tracking method is perturb and observe (P&O) due to its simplicity and ease of implementation. The P&O method operates as follows: the solar panel voltage is perturbed by adjusting the duty cycle of the boost converter; if the output power increases, the voltage is perturbed again in the same direction, otherwise it is perturbed in the opposite direction. Each perturbation of the duty cycle is called a step. This section investigates the performance of the custom MPPT with two types of P&O tracking algorithms, fixed step (FS) and adaptive step (AS).

FS size is the most basic and easy to implement. It has a fixed duty cycle step size (Δd) which makes tuning very simple [18] however requires a trade-off between response time and MPP power loss. A large step size gives fast convergence, but results in power loss due to oscillations around the MPP. To minimize oscillation losses, the smallest Δd (Δd_{min}) that results in a ΔV greater than the ripple voltage is used [17]. Following this process, $\Delta \text{d}_{\text{min}}$ for the given design is 0.254%.

An adaptive step size attempts to remedy the issues of fixed step by scaling the step size with the derivative of power with respect to voltage and a scaling factor N [17],

$$\Delta d = N \frac{\Delta P}{\Delta V} \tag{8}$$

where Δd is the step size, ΔP is the change in power, and ΔV is the change in panel voltage. The scaling factor should be tuned for optimal performance as in [18].

The solar array, custom MPPT, and battery system for one wing section were modeled using the SimElectronics libraries in Simulink. The simulated system consisted of 8 series connected SunPower E60 solar cells, 8 Panasonic NCR18650B batteries connected in a 2p4s configuration, and the custom MPPT modeled with non-ideal components. The tracking algorithm was implemented using a timed controller which ran and updated the duty cycle every 1 ms. Additionally, the controller sampled the array voltage and current in the same super-sample method as the actual MPPT board. This super-sample method is the average of two 12-bit quantized samples of the array voltage and current taken 150 μs apart. A super-sample was taken every 239 μs. The Simulink block diagram can be seen in Figure 13.

Four simulations were run, FS with 0.254 and 0.5 step sizes and AS with 0.1 and 0.5 scaling factors. Both algorithms were simulated in dynamic solar irradiance conditions that correspond to the worst-case scenario of quad-rotor mode turning 180° on its z axis in 85 ms. The results of each simulation is shown in Table III and Figure 14.

Fixed Step (Δd_1=0.254%)	0.2746 J
Fixed Step (Δd_2=0.5%)	0.7813 J
Adaptive Step (N_1=0.5)	1.3216 J
Adaptive Step (N_2=0.1)	1.1866 J

TABLE III: Net energy from dynamic irradiance over 85 ms.

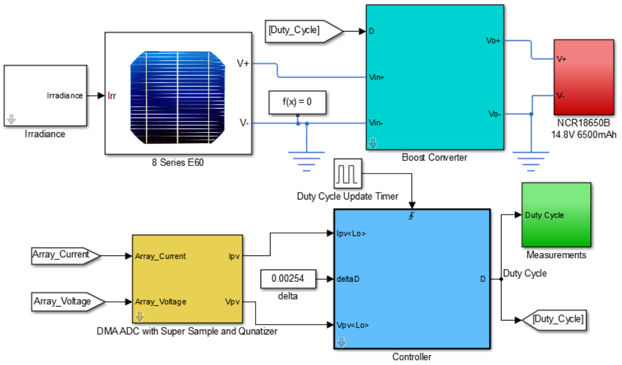

Fig. 13: General Simulink block diagram including solar array, batteries, boost converter, super-sample quantizer, and timed controller.

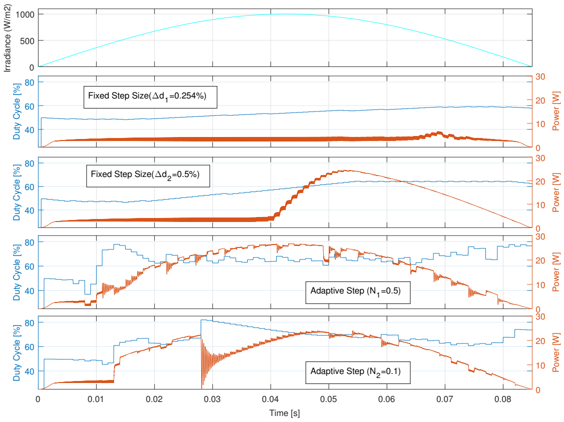

Fig. 14: Simulated tracking algorithm response to dynamic irradiance.

Table III indicates that the FS (Δd_1=0.254%) algorithm cannot respond fast enough, and, although FS (Δd_2=0.5%) was able to collect three times more energy, both AS algorithms collected at least five times more energy. While it is unlikely that solar irradiance will be as volatile in practice as in the simulation, maximizing energy collection in dynamic conditions is critical due to the flight characteristics of a transformable aircraft. Furthermore, flight data can be integrated into the power tracking system through adjusting the sensitivity of an AS algorithm through the scaling factor N.

III. EXPERIMENTAL TESTS

A. Hybrid Propulsion System

In order to empirically confirm the optimization behavior of the hybrid propulsion system proposed in Section II-B, a testbed was designed and constructed to perform tests under the static thrust case. Sheets of laser-cut acrylic were assembled to make a class-three lever to measure thrust applied at the end of the arm. A Himax HC2816-0890 outrunner motor was paired with a VPP101 Pro pushrod-style variable pitch assembly. An APC 10x4.7SF propeller was modified to attach to the assembly, and a Futaba S3156 digital servo motor actuated the blade pitch. Thrust was measured by resting the lever arm on a TAL201 10 kg load cell, and the pitch of the propeller was calculated via the servo angle by measuring the commanded position of the servo motor. Voltage across the motor was obtained by recording the pulse width of the throttle signal into the electronic speed controller. Power consumption was measured using a MAX9611 current sense amplifier, and motor speed was measured with a custom-built infrared tachometer. These sensors were interfaced with an Atmega328P and sensor data was stored on a microSD card.

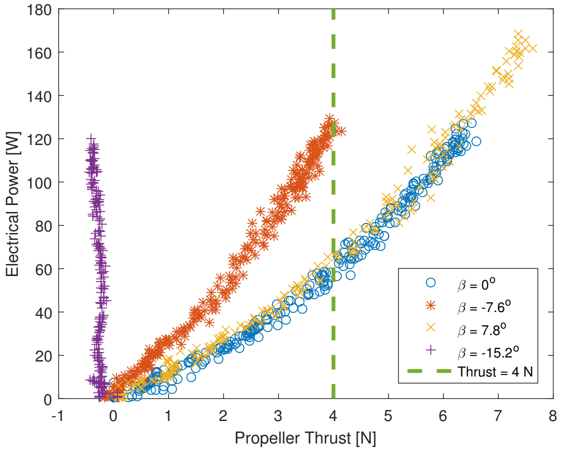

Fig. 15: Shown here is a succession of tests performed under static thrust conditions to approximate hover in quad-rotor mode. While β = -7.6 ° will produce 4 N of thrust at 120 W, the same amount of thrust can be achieved with only 60 W when β = 0 °.

Figure 15 illustrates the influence of the blade pitch offset angle β on the ability of a propulsion system to efficiently produce thrust in a given flight condition. Such flexibility in the propulsion system will allow power to be efficiently converted into thrust across the entire flight envelope.

B. Power Electronics

Figure 16 shows the efficiency of the custom MPPT operating as a boost converter (i.e. with no tracking algorithm) at 100 kHz switching frequency and various input voltages and duty ratios. A 9.4 Ω power resistor was used as a load, dissipating approximately 30 W at 16.8 V. The input voltages were supplied with a Rigol DP1116A programmable DC power supply. Measurements were made using the MPPT's on-board ADCs and TI INA212 current sense amplifiers.

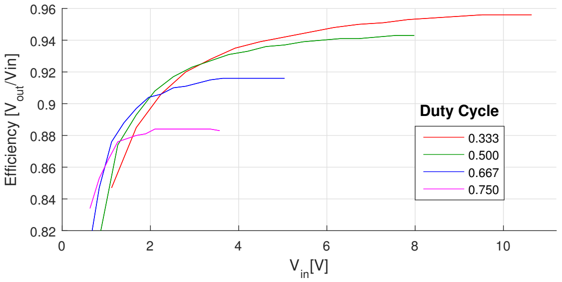

Fig. 16: Efficiency of custom MPPT operating at 100 kHz switching frequency.

The results demonstrate that high efficiency (>90%) can be achieved with a basic (non-synchronous) topology. For higher efficiency, either the battery voltage can be lowered or the number of solar cells in series can be increased [16].

Ideally, the input voltage should be as close as possible to the output voltage to maximize switch utilization. A synchronous topology can also be used to avoid diode forward voltage loss. Soft-switching techniques can further reduce switching losses. Figure 17 shows the efficiency, input, and output power of the LT8490 MPPT connected to the fixed-wing SUAV:Q. At an ideal angle of incidence, the LT8490 MPPT is capable of operating with efficiency in excess of 97%, however the limitations of this single high power MPPT are visible in the transitional low power levels. Since this MPPT, like the vast majority of commercially available MPPTs, was designed for relatively high voltage of 17V to 55V and power up to 250 W, it has poor performance at low voltage power levels, dropping to below 75% efficiency. As discussed in Section II-D, these losses can be largely minimized by designing MPPT hardware for low power applications.

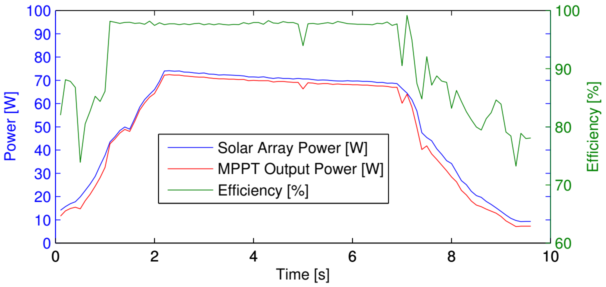

Fig. 17: Power measured with an array of 32 SunPower E60 solar cells affixed to the SUAV-Q while in a fixed-wing configuration. The solar array was connected to a LT8490 MPPT development board and the output connected to a 1p4s 3600 mAh lithium polymer battery in parallel with a 2 Ω resistive load.

IV. CONCLUSIONS AND FUTURE WORK

Presented in this paper is the extended development of the SUAV:Q platform. The design for a modular payload bay was presented and prototyped. Conditions necessary to achieve stable flight for varying payload mass and center of gravity location were discussed.

A comprehensive analysis of the propulsion system was evaluated, comparing the efficiency of a fixed pitch propulsion system to that of a variable pitch system. Results from numerical simulations and experimental tests showed that dramatic increase in propulsion efficiency is possible through optimal control of a propeller's pitch angle. Future work will involve designing a controller to minimize power consumption in real-time by varying the VPP across both quad-rotor and fixed-wing states.

Finally, the design for a small, high efficiency custom solar MPPT for the SUAV:Q was presented. A performance evaluation of tracking algorithms was simulated and the hardware design realized on a 4-layer PCB with conversion efficiencies >90% across the target power range. Solar power data was collected using an off-the-shelf LT8940 MPPT which exhibited low converter efficiency at the target power level, further justifying the need for a custom designed MPPT. The custom hardware lends itself for future redesign to take advantage of new technologies, such as gallium nitride power transistors, and utilization of system wide interleaved topology. Lastly, the modular firmware allows for new tracking methods to be tested such as flight data integration, state estimation, and optimal control techniques.

V. ACKNOWLEDGEMENTS

This material is based upon work supported by the National Science Foundation through grants #IIP-0934327, #IIS-1017344, #IIP-1332133, #IIS-1427014, #IIP-1432957, #OISE-1551059, #CNS-1514626, #CNS-1531330, and #CNS-1544887. Ruben D'Sa was supported by a National Science Foundation Graduate Research Fellowship No. 00039202.

REFERENCES

[1] R. D'Sa, D. Jenson, and N. Papanikolopoulos, "SUAV:Q - A Hybrid Approach To Solar-Powered Flight," *IEEE International Conference on Robotics and Automation (ICRA)*, pp. 3288–3294, May 2016.

[2] M. A. Khan, M. A. Zondlo, and D. J. Lary, "Open-Path Greenhouse Gas Sensor for UAV applications," in *Conference on Lasers and Electro-Optics*, vol. 6, no. 1, June 2012, pp. 1–2.

[3] C. Flener, M. Vaaja, A. Jaakkola, A. Krooks, H. Kaartinen, A. Kukko, E. Kasvi, H. Hyyppa, J. Hyyppa, and P. Alho, "Seamless Mapping of River Channels at High Resolution Using Mobile LiDAR and UAV-Photography," in *Remote Sensing*, vol. 12, no. 4, November 2013, pp. 6382–6407.

[4] D. Zermas, D. Teng, P. Stanitsas, M. Bazakos, V. Morellas, D. Mulla, and N. Papanikolopoulos, "Automation Solutions for the Evaluation of Plant Health in Corn Fields," in *IEEE/RSJ International Conference on Intelligent Robots and Systems (IROS), Hamburg*, September 2015, pp. 6521–6527.

[5] R. Deits and R. Tedrake, "Efficient mixed-integer planning for UAVs in cluttered environments," in *IEEE International Conference on Robotics and Automation (ICRA)*, May 2015, pp. 42–49.

[6] A. Noth, W. Engel, and R. Siegwart, "Design of an ultra-lightweight autonomous solar airplane for continuous flight," in *Field and Service Robotics*, ser. Springer Tracts in Advanced Robotics, vol. 25. Springer Berlin Heidelberg, 2006, pp. 441–452.

[7] P. Oettershagen, A. Melzer, T. Mantel, K. Rudin, R. Lotz, D. Siebenmann, S. Leutenegger, K. Alexis, and R. Siegwart, "A solar-powered hand-launchable UAV for low-altitude multi-day continuous flight," in *IEEE International Conference on Robotics and Automation (ICRA)*, May 2015, pp. 3986–3993.

[8] S. Morton, R. D'Sa, and N. Papanikolopoulos, "Solar Powered UAV: Design and Experiments," in *IEEE/RSJ International Conference on Intelligent Robots and Systems (IROS), Hamburg*, vol. 14, no. 1, 2015, pp. 2460–2466.

[9] A. S. Saeed, A. B. Younes, S. Islam, J. Dias, L. Seneviratne, and C. Guowei, "A review on the platform design, dynamic modeling and control of hybrid UAVs," in *International Conference on Unmanned Aircraft Systems (ICUAS)*, June 2015, pp. 806–815.

[10] A. Deperrois, "Stability analysis using XFLR5," http://www.xflr5.com/docs/XFLR5_and_Stability_analysis.pdf, 2010.

[11] R. A. McDonald, "Optimal propeller pitch scheduling and propeller-airframe matching for conceptual design," in *AIAA Aviation Technology, Integration, and Operations Conference*, June 2015, p. 3190.

[12] B. Brandt, John and M. Selig, "Propeller Performance Data at Low Reynolds Numbers," in *49th AIAA aerospace sciences meeting*, vol. 20, July 2011, pp. 2011–1255.

[13] M. Drela, "QPROP Formulation," http://web.mit.edu/drela/Public/web/qprop/qprop_theory.pdf, 2006.

[14] I. Waitz, "Aircraft Performance," http://ocw.mit.edu/ans7870/16/16.unified/propulsionS04/UnifiedPropulsion4/UnifiedPropulsion4.htm, 2003.

[15] M. Drela and H. Youngren, "Subsonic Airfoil Development System," http://web.mit.edu/drela/Public/web/xfoil/, 2013.

[16] N. Mohan, *Power Electronics: A First Course*. Wiley, 2012.

[17] N. Femia, G. Petrone, G. Spagnuolo, and M. Vitelli, *Power Electronics and Control Techniques for Maximum Energy Harvesting in Photovoltaic Systems*. CRC Press, 2012.

[18] ——, "Optimization of perturb and observe maximum power point tracking method," in *IEEE Transactions on Power Electronics*, vol. 20, no. 4, July 2005, pp. 963–973.